Joule

Article

Areal uniformity enables scaled separator-based CO electrolyzers

Graphical abstract

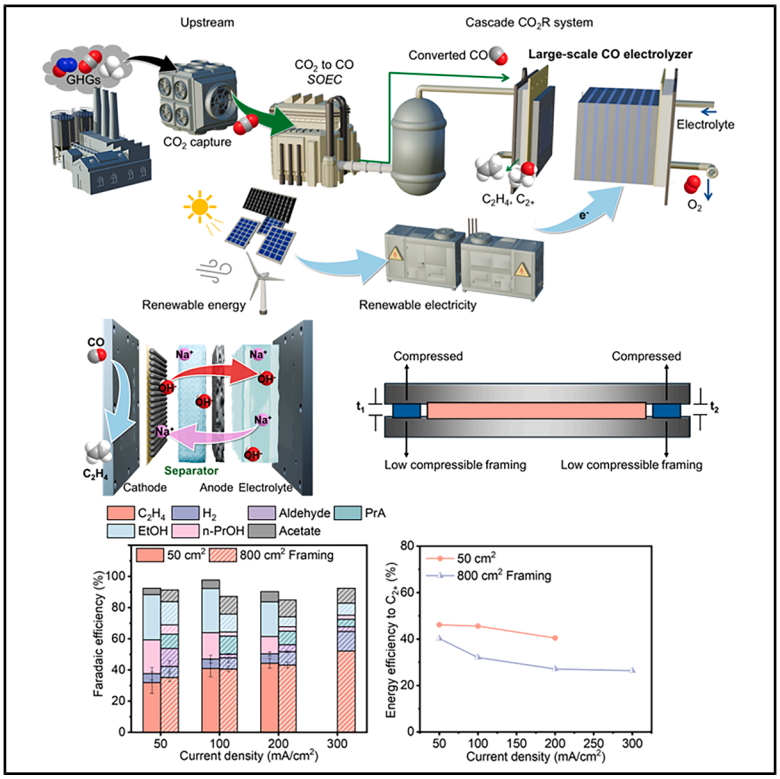

Highlights

- A framing setup for scaling a separator-based CO electrolyzer with uniform compression
- Approach demonstrated in an 800 cm^2 single cell, the largest single cell area for CO-to-C_2H_4
- Total C_2H_4 current of 125 A, 52% C_2H_4 FE, and 192 A total partial current to C_{2+} products

Authors

Puhua Sun, Colin P. O'Brien, Hyun Sik Moon, ..., Rui Kai Miao, Edward H. Sargent, David Sinton

Correspondence

ruikai.miao@mail.utoronto.ca (R.K.M.), dave.sinton@utoronto.ca (D.S.)

In brief

Industrial-scale electrochemical CO reduction faces mechanical challenges that hinder performance. We demonstrate a separator-based CO electrolyzer operating at 800 cm^2 using a rigid framing support that enables uniform compression across the active area. The single-cell device achieves 125 A of ethylene current at 52% Faradaic efficiency and retains ~65% of the bench-scale energy efficiency, suggesting a practical route toward large-area CO electrolysis.

Sun et al., 2026, Joule *10*, 102441
September 16, 2026
https://doi.org/10.1016/j.joule.2026.102441

CellPress

Joule

CellPress

Article

Areal uniformity enables scaled separator-based CO electrolyzers

Puhua Sun,[1] Colin P. O'Brien,[6] Hyun Sik Moon,[1,2] Tevin Devasagayam,[1] Yuxuan Gao,[1] Roozbeh Alishahian,[1] Haoyang Deng,[1] Panagiotis Papangelakis,[1] Jieyuan Liu,[1] Jiexin Zhu,[1] Qian Sun,[1] Zunmin Guo,[1] Prasad V. Sarma,[1] Tanushree Ghosh,[1] Yuxuan Che,[1] Chengqian Wu,[1] Qiyou Wang,[1] Jeff Parkey,[5] Jonathan Raisin,[4,5] Shaffiq Jaffer,[1,5] Cao-Thang Dinh,[3] Rui Kai Miao,[1,*] Edward H. Sargent,[2] and David Sinton[1,7,*]

[1]Department of Mechanical and Industrial Engineering, University of Toronto, Toronto, ON, Canada
[2]Department of Electrical and Computer Engineering, University of Toronto, Toronto, ON, Canada
[3]Department of Chemical Engineering, Smith Engineering, Queen's University, Kingston, ON, Canada
[4]SUNCAT Center for Interface Science and Catalysis, Department of Chemical Engineering, Stanford University, Stanford, CA, USA
[5]TotalEnergies E&P Research & Technology USA, LLC, Houston, TX, USA
[6]CERT Systems Inc, Toronto, ON, Canada
[7]Lead contact
*Correspondence: ruikai.miao@mail.utoronto.ca (R.K.M.), dave.sinton@utoronto.ca (D.S.)
https://doi.org/10.1016/j.joule.2026.102441

CONTEXT & SCALE Electrochemical methods of converting carbon monoxide into multi-carbon products, such as ethylene, hold potential as a path to low-carbon fuels and chemical feedstocks, particularly if the method includes upstream CO production from captured CO_2. While the field has seen substantial laboratory-scale advances, efficient CO reduction at an industrial scale has remained elusive. Electrolyzer cells must be made to operate more efficiently and reliably across active areas spanning hundreds or even thousands of square centimeters. At these scales, mechanical and electrical inconsistencies pose a considerable challenge. Separator-based electrolyzers enable high energy efficiency and are structurally robust, but scaling introduces new problems. In this work, we focus on overcoming an important mechanical limitation in such a setup by using a rigid framing support to maintain uniform compression in an 800 cm^2 electrolyzer. Demonstrating stable, high-current ethylene production at this scale suggests a viable route to CO electrolysis at an industrial scale.

SUMMARY

Electrochemical CO reduction (COR) to multi-carbon products enables low-carbon fuels and chemicals, particularly when coupled with efficient upstream CO generation from CO_2. Industrial implementation will require efficient operation over large areas, on the order of 100–1,000 cm^2 per cell. Separator-based electrolyzers combine high energy efficiency with greater mechanical robustness than anion exchange membrane (AEM) cells, making them well suited for large-area operation. At 800 cm^2, however, non-uniform compression across the active area led to puncture of the separator, localized short circuit, and losses in current and efficiency. Protective spacers used in prior large-area designs can shield thin components but add ohmic resistance and cell voltage. We engineer a rigid framing support that preserves areal uniformity across the active area of the scaled separator-based electrolyzer. We thus report an 800 cm^2 single-cell COR electrolyzer delivering 125 A total ethylene current at 52% Faradaic efficiency and retaining ~65% of the bench-scale energy efficiency.

INTRODUCTION

Electrochemical reduction of CO_2 (CO_2R) can convert CO_2 emissions into valuable multi-carbon (C_{2+}) fuels and chemicals.[1] When powered by low-carbon electricity, CO_2R can contribute to the decarbonization of chemical production.[2–4]

Substantial progress at laboratory-scale CO_2R (<10 cm^2 active areas) now enables ethylene (C_2H_4) Faradaic efficiencies (FEs) exceeding 50% and total C_{2+} FE surpassing 90% at high current densities (>100 mA/cm^2).[5–7] The field has also addressed carbonate formation, achieving single-pass CO_2 conversion efficiencies above 80%.

Among electrosynthesis approaches, a particularly promising strategy is cascade CO_2R, which combines CO_2-to-CO conversion followed by CO reduction (COR), leveraging mature, industrially available CO_2-to-CO technologies.[8–10] Unlike CO_2, CO

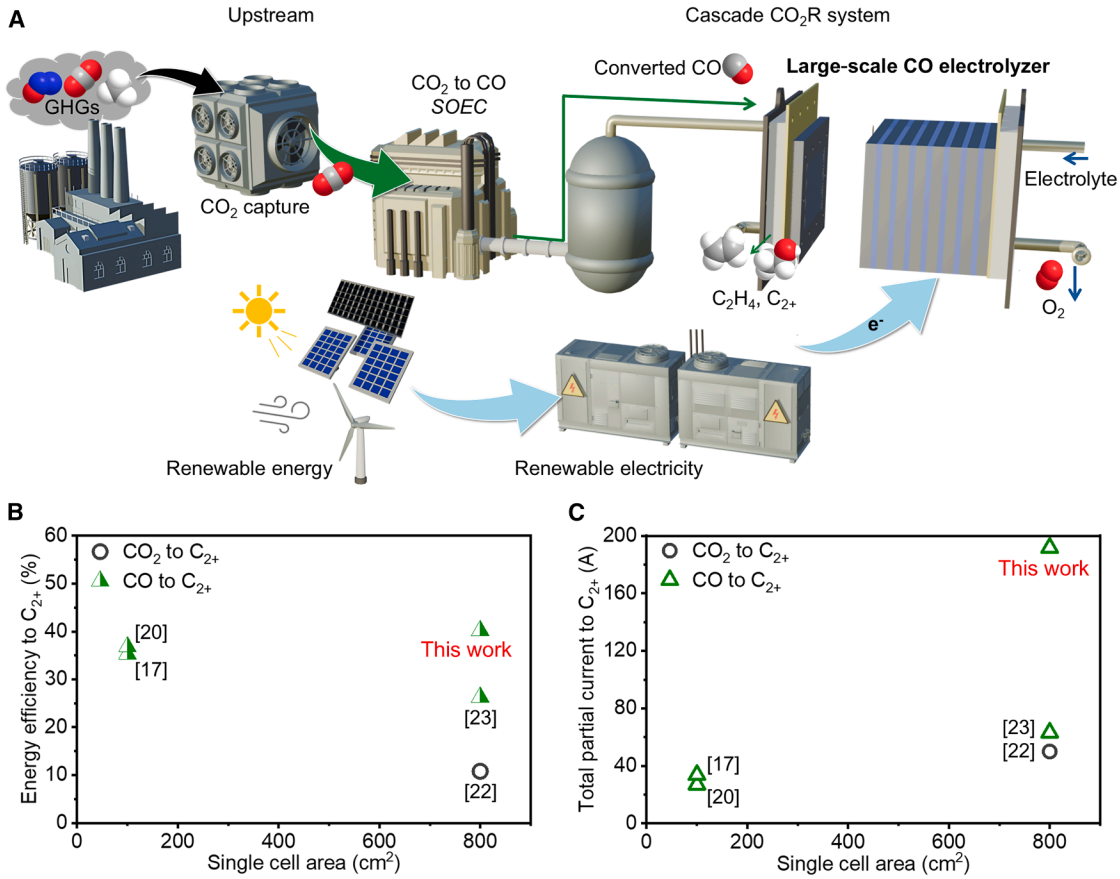

Figure 1. Schematic of cascade CO_2R and results comparison

(A) Schematic illustration of the cascade CO_2R process and the associated scaling strategy.

(B) Comparison of EE toward C_{2+} products reported in the literature versus this work.

(C) Comparison of total partial current to C_{2+} products reported in the literature versus this work.[16–22]

does not react with hydroxide, enabling stable COR operation in alkaline conditions that favor C–C coupling kinetics and minimize Nernstian pH losses. COR integrates effectively into a zero-gap membrane electrode assembly (MEA), reducing ohmic resistance and offering scalability. State-of-the-art COR systems have demonstrated C_2H_4 FE exceeding 80%, near-complete selectivity for C_{2+} products, and full-cell voltages ~2.5 V—corresponding to energy efficiencies (EEs) >35% for C_2H_4 and >40% for C_{2+} products.[2,11–15]

These advances make scaling COR systems to industrially relevant sizes increasingly attractive (Figure 1A). Several studies report CO_2 and CO electrolyzers with single-cell active areas of 50–100 cm^2 that match <10 cm^2 performance.[16,20,21,23–27] However, industrial electrolyzers typically target much larger cells; for example, water-electrolysis stacks operate ~1,000 cm^2 per cell with hundreds of cells per stack, consuming megawatts of electricity.[16,28–30] Scaling challenges—including maintaining uniform current distribution, effective mass transport, heat management, and mechanical stability—increase exponentially with electrode area, often resulting in performance losses. Previous CO_2/COR demonstrations at 800 cm^2 showed partial currents limited to 20 A for C_2H_4, and 60 A for C_{2+} products.[23] We therefore aim to scale COR electrolysis beyond existing demonstrations—targeting high EE at elevated partial current (Figures 1B and 1C).[16–21]

RESULTS

Maintaining performance during scale-up to 50 cm^2

Membrane selection strongly impacts COR performance due to differing ion transport behavior, product crossover, and water management. We began by benchmarking the system in a MEA configuration at 1 cm^2 (Figures S1 and S2), using a copper oxide (CuO) cathode and IrO_x anode,[25] and different membrane types to assess their effects on performance (Figures 2A–2C).[26]

Cation exchange membranes (CEMs) facilitate proton and cation transport and typically offer higher conductivity and mechanical robustness (Figure 2A) than anion exchange membranes (AEMs).[19,23,27] These advantages have enabled CEM-based COR systems to scale-up to 800 cm^2 for alcohol production, effectively mitigating product crossover. However, CEMs tend to promote hydrogen evolution reaction (HER) due to increased proton availability and water drag at high current

Please cite this article in press as: Sun et al., Areal uniformity enables scaled separator-based CO electrolyzers, Joule (2026), https://doi.org/10.1016/j.joule.2026.102441

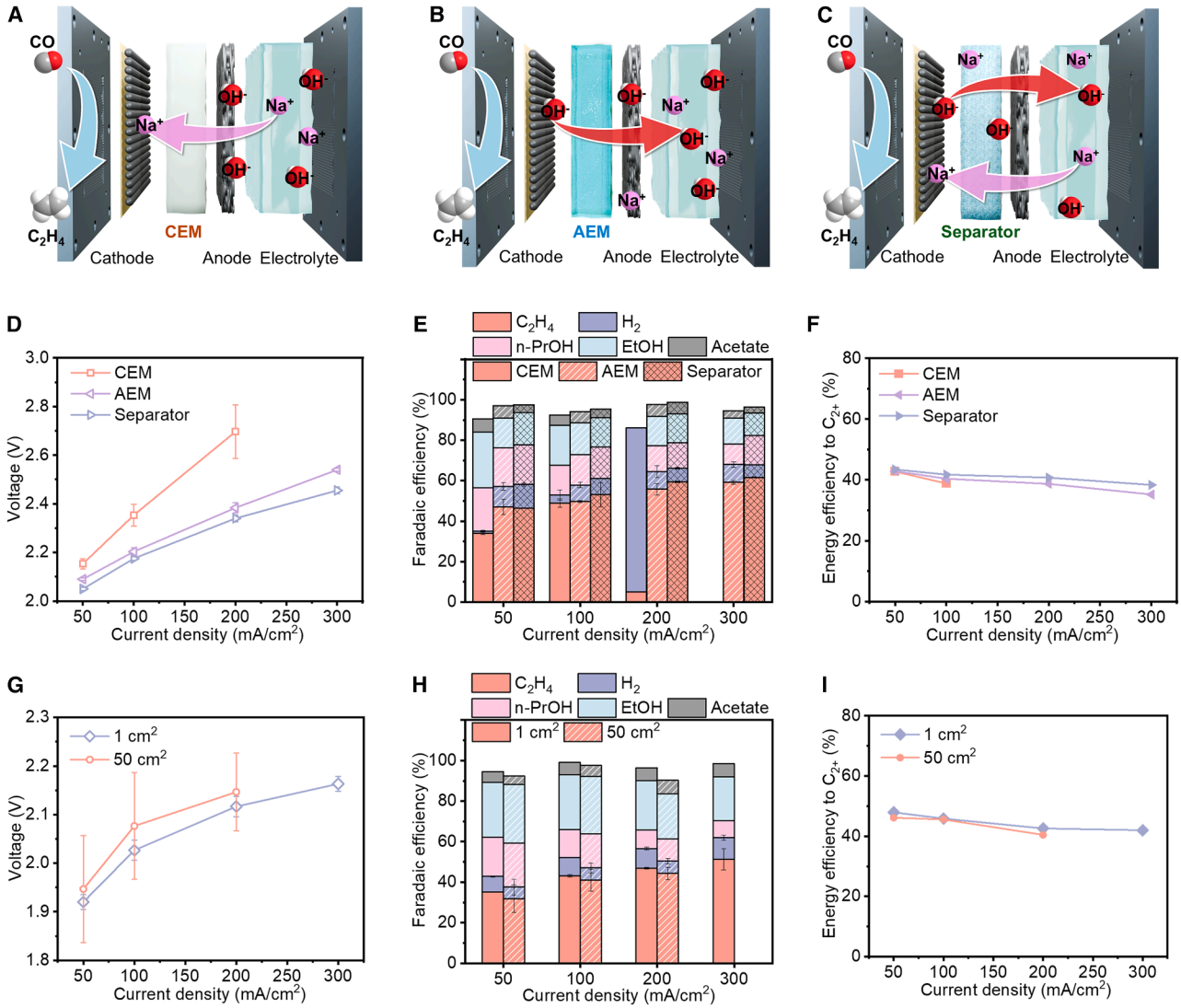

Figure 2. Comparison of CEM-, AEM-, and separator-based systems and scaling from 1 to 50 cm^2

(A–C) Schematic illustration of (A) CEM system, (B) AEM system, and (C) separator system.

(D and G) Full-cell voltage (D) in CEM, AEM, and separator systems, and (G) in 1 and 50 cm^2 separator systems.

(E and H) FE to all products (E) in CEM, AEM, and separator systems, and (H) in 1 and 50 cm^2 separator systems.

(F and I) EE to C_{2+} products (F) in CEM, AEM, and separator system, and (I) in 1 and 50 cm^2 separator systems.

Experimental conditions in (D)–(F): 1 mg/cm^2, same batch of commercial CuO (Sigma), spraying on the same commercial carbon paper (H23C3 from Fuel Cell Store); anode: IrO_x; membranes: CEM (Nafion 117), AEM (Sustainion 37–50), Separator (PTFE unlaminated membrane filters, hydrophilic, 1.0 micron); electrolyte: 2 M NaOH.

Experimental conditions in (G)–(I): 1 mg/cm^2, same batch of commercial CuO (Sigma), spraying on the same commercial carbon paper (H23C3 from Fuel Cell Store); anode: NiFe-Ni foam; membrane: Separator (PTFE unlaminated membrane filters, hydrophilic, 1.0 micron); electrolyte: 2 M NaOH.

densities. At 100 mA/cm^2, we achieved 88% C_{2+} FE at a full-cell voltage of 2.4 V, corresponding to a C_{2+} EE of 39%. However, flooding quickly occurred at current densities exceeding 200 mA/cm^2, reducing C_{2+} EE to ~7.4% (Figures 2D–2F).

In contrast, AEMs transport hydroxide from cathode to anode, and thereby reduce flooding and improve FE (Figure 2B).[1] At 200 mA/cm^2, the AEM-based cell achieved 89% C_{2+} FE at a full-cell voltage of 2.4 V (C_{2+} EE of 38%) and sustained this performance at higher current densities (Figures 2D–2F).

Uncharged hydrophilic separators enable efficient, ambipolar ion transport through the bulk alkaline electrolyte (Figure 2C). Recent studies show such separators can deliver higher EE than AEM-based CO_2R/COR systems.[15,31–35] Positioned between the electrodes, these separators can effectively block gas crossover to the opposite electrodes. We therefore evaluated a hydrophilic polytetrafluoroethylene (PTFE) separator for electrode separation. At 200 mA/cm^2, the separator-based MEA achieved 92% C_{2+} FE at a

full-cell voltage of 2.3 V, corresponding to a C_{2+} EE of 41% (Figures 2D–2F).

Incorporating a hydrophilic separator also offers practical advantages over AEMs for scale-up: separators can provide greater mechanical strength and retain structural integrity even when dry, simplifying handling and cell assembly. We thus selected the separator-based system for scaling high-performance COR. We further optimized the anode by loading NiFe onto Ni foam, achieving further ~200 mV improvement in full-cell voltage at 200 mA/cm^2, which led to an improved EE (Figure S3). Owing to its lower voltage and cost, we adopted this NiFe-Ni foam anode for scaling from 1 to 50 cm^2, and ultimately to 800 cm^2.[25,36–44]

As an intermediate step, we expanded the system to a 50 cm^2 active area using the same electrode materials and PTFE separator (Figures S1 and S4). The cell featured a four-channel serpentine flow field with channel dimensions matched to those used in the 1 cm^2 system to maintain comparable pressure drops and ensure uniform gas delivery. The 50 cm^2 cell showed no loss in performance, achieving a C_{2+} FE of 84% at a full-cell voltage of 2.2 V at 200 mA/cm^2, corresponding to a C_{2+} EE of 41%. These results demonstrate that the system could be moderately scaled without compromising performance (Figures 2G–2I).

We further evaluated temperature effects using 1 and 50 cm^2 cells operated between 25°C and 60°C. As the temperature increased from 25°C to 50°C, C_2H_4 FE increased slightly but declined at 60°C (Figure S5A). Over the same range, the full-cell voltage decreased by ~0.12 V (Figure S5B).

Scaling challenges with the 800 cm^2 cell

We next scaled the system to an 800 cm^2 active area (20 cm × 40 cm), a size chosen based on commercially available electrode and membrane dimensions. The cell has an eight-channel serpentine flow field designed to balance pressure drop and ensure uniform reactant/product distribution to the catalyst.[45–47] The cell was sealed with a sealing ring, consistent with the approach used in the 1 and 50 cm^2 setups (Figures 3A, 3B, S4, S6, and S7). During assembly, we applied a uniform torque of ~40 N·m.

Initial tests at this scale showed poor performance, with the highest observed C_2H_4 FE being 23% at 200 mA/cm^2 (Figures 3E–3G). In addition to low selectivity, we observed unusually low full-cell voltages at low current densities (<1.9 V at 50 mA/cm^2), which sharply increased with the current, exceeding 2.4 V at 300 mA/cm^2.

Quantification of liquid products (Figures S8 and S9) showed that the total FE across all products summed to only ~50%, with no significant gas product crossover detected between electrodes (Figure S10A). Thus, nearly half of the applied current was unaccounted for. The oxygen evolution reaction (OER) rate at the anode likewise reached only ~50% of the theoretical value (Figure S11), suggesting the cause was systemic current loss from localized short circuits, affecting both electrodes, rather than analytical limitations.

Upon disassembly, we observed punctures in the separator that we suspect created unintended current pathways (Figure S12), causing localized thermal damage on electrodes and flow plates at low-resistance spots (Figure S13). These short circuits likely contributed to the low full-cell voltages and reduced FE at low current densities. As the current density increased, a greater fraction of the current was forced through the electrochemical path, modestly improving FE and increasing voltage, but overall performance remained well below that of smaller cells.

Repeated tests consistently showed low FE trends, although both voltage and total FE varied considerably across three independent trials (Figure 3E), indicating challenges in achieving uniform areal pressure across the large electrode area during assembly. We lowered the compression torque (28–34 N·m) to prevent puncturing the separator; however, this caused sealing failures, electrolyte leakage, and low FE and short-circuiting persisted (Figure S14).

To assess compression uniformity, we measured variations in the cell thickness at multiple locations before and after assembly. The thickness changes revealed uneven compression, with certain edges showing considerably greater thickness differences—indicating higher local compression—whereas other areas showed smaller changes. Pressure-sensitive film measurements showed similar non-uniformity, with one side more compressed than the other (Figures S15 and S16; Table S1). In contrast, pressure distribution appeared uniform in the 1 and 50 cm^2 electrolyzers under similar testing (Figures S17 and S18).

We hypothesized that the sealing ring along its perimeter—a narrow line of contact around the cell edge—does not offer sufficient mechanical support across the large 800 cm^2 active area. While effective for smaller cells, this perimeter-only sealing makes the system highly sensitive to small assembly variations, causing uneven compression, which we attributed to performance losses. Regions experiencing excessive pressure can locally puncture the thin (~50 μm) separator, while other areas suffer from insufficient compression, resulting in poor interfacial contact and gas or electrolyte leakage. Membrane puncture is a common issue in prior large-scale studies using thin (~50 μm) AEMs sealed with sealing rings.[22,45,46] Spacers between the AEM and the anode have been used to provide mechanical support and prevent membrane puncturing; however, these spacers increased ohmic resistance, raising cell voltage and reducing overall efficiency.[22,45,46]

Overcoming compression challenges for reliable large-scale COR

To avoid the added ohmic resistance associated with spaces—and thereby to improve EE—we explored a flat compliant gasket (Young's Modulus ~0.0036 GPa)[48] as an alternative sealing method (Figures 3, S19, and S20). Gaskets are a common mechanical sealing solution in industrial applications such as piping, machinery, and pressure vessels because their elastic compliance accommodates surface irregularities and assembly tolerances.[14,49–51] Compared with perimeter sealing rings, the gasket provides larger-areal mechanical support and greater tolerance to assembly variations, which is especially important for protecting thin-cell components. To accommodate the increased gasket thickness while maintaining proper compression and electrical connectivity of all electrode components, we introduced an additional support current collector layer

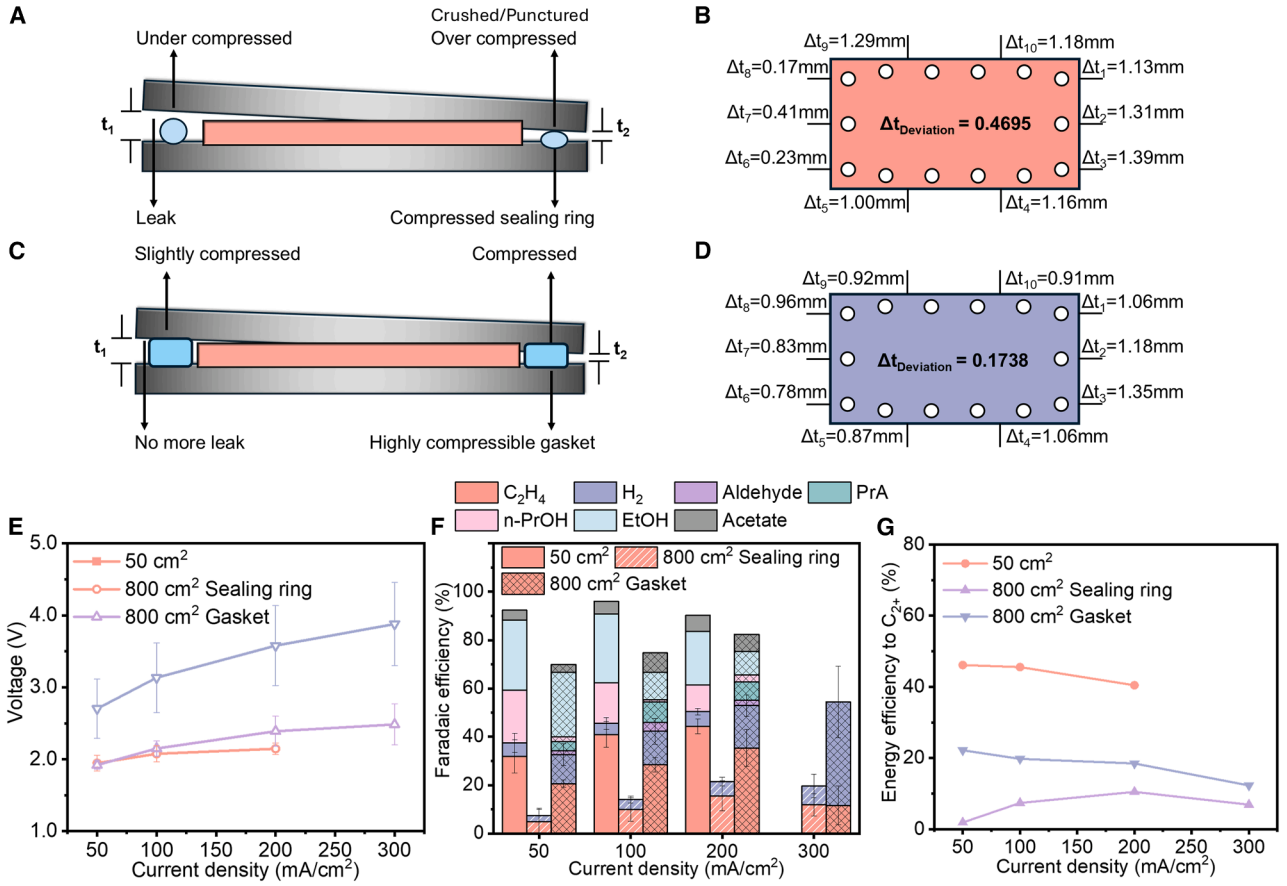

Figure 3. Scaling from 50 to 800 cm^2 with sealing ring and gasket setup

(A and C) Configuration of (A) using a sealing ring, and (C) using a compressible gasket in an 800 cm^2 separator-based system.

(B and D) The thickness at different spots across the cell of (B) the sealing ring, and (D) the gasket in an 800 cm^2 separator-based system.

(E) Full-cell voltage in 50 cm^2, 800 cm^2 with sealing ring setup, and 800 cm^2 with gasket setup.

(F) FE toward all products in 50 cm^2, 800 cm^2 with a sealing ring setup, and 800 cm^2 with a gasket setup.

(G) EE to C_{2+} products at 50 cm^2, 800 cm^2 with a sealing ring setup, and 800 cm^2 with a gasket setup.

Experiment conditions: cathode: 1 mg/cm^2, same batch of commercial CuO (Sigma) spraying on same commercial carbon paper (H23C3 from Fuel Cell Store); anode: NiFe-Ni foam; membrane: separator (PTFE unlaminated membrane filters, hydrophilic, 1.0 micron from Sterlitech); electrolyte: 2 M NaOH.

compressed together with the electrodes and separator (Figures S15B and S21).[24]

Pressure-sensitive film tests with the gasket showed improved pressure uniformity across the cell. We observed an improved total FE of 82%, with 65% C_{2+} FE and a full-cell voltage of 3.6 V at 200 mA/cm^2, corresponding to a C_{2+} EE of 19% (Figures 3E–3G). We again measured variations in cell thickness at multiple points before and after assembly across the large electrode area. While improved, some uneven compression remained, which we attributed to the gasket's compressibility that, while providing better overall support, still allowed localized areas of higher or lower compression (Figure 3C).

To further address this compressibility issue, we designed a framing support (Figures S22 and S23) made of PTFE (Young's Modulus ~0.5 GPa),[52,53] which has a higher resistance to elastic deformation under compression. The rigid PTFE frame applies targeted compression at the non-active edge regions to ensure proper sealing, while maintaining moderate and uniform compression across the 800 cm^2 active area. Measurements of cell thickness variations before and after assembly showed consistency across the entire area, and pressure-sensitive film indicated uniform pressure distribution compared with all other sealing methods (Figures 4A, 4B, and S15C).

With the 800 cm^2 framing setup, we obtained a total FE of ~90%, with 78% C_{2+} FE, and a full-cell voltage of 3.0 V at 200 mA/cm^2 (total current of 160 A), corresponding to a C_{2+} EE of 27%. The system retained 65% of its initial value of C_{2+} EE when scaling from 1 to 800 cm^2 at 200 mA/cm^2, demonstrating that high performance can be sustained through careful system optimization and that mechanical cell architectures are scale-specific (Figures 4C–4E). This setup also delivered 52% C_2H_4 FE, 80% C_{2+} FE, and a full-cell voltage of 3.2 V at 300 mA/cm^2 (total current of 160 A).

The efficiency shortfall arises mainly from the higher voltage at scale. To probe the origin of this voltage penalty, we performed

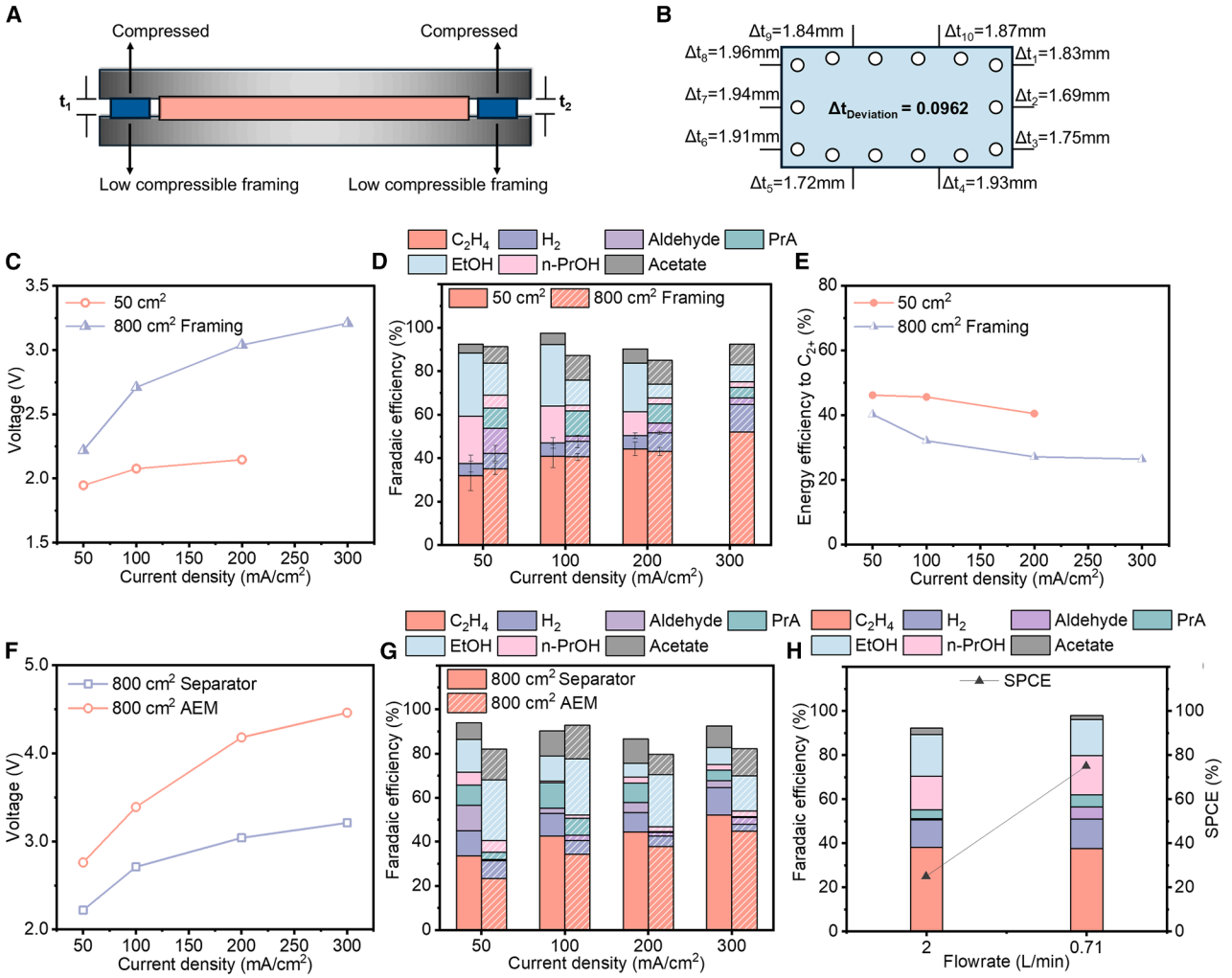

Figure 4. Optimization with PTFE framing setup in an 800 cm^2 cell and performance comparison

(A) Configuration using PTFE framing in an 800 cm^2 MEA system.

(B) Thickness at different spots across the cell in the PTFE framing 800 cm^2 MEA system.

(C and F) Full-cell voltage (C) in the 50 and 800 cm^2 cell with PTFE framing, and (F) in the separator-based and AEM-based 800 cm^2 cell with PTFE framing.

(D and G) FE to all products (D) in the 50 cm^2 cell and 800 cm^2 cell, and (G) in the separator-based and AEM-based 800 cm^2 cell with PTFE framing.

(E) EE to C_{2+} products at 50 cm^2 cell and 800 cm^2 cell with PTFE framing.

(H) The FE to all products and SPCE under different flow rates in an 800 cm^2 separator system with the PTFE framing setup.

Experiment conditions: cathode: 1 mg/cm^2, same batch of commercial CuO (Sigma), spraying on the same commercial carbon paper (H23C3 from Fuel Cell Store); anode: NiFe-Ni foam; membrane: separator (PTFE unlaminated membrane filters, hydrophilic, 1.0 micron from Sterlitech); electrolyte: 2 M NaOH.

electrochemical impedance spectroscopy (EIS) measurements for the 800 cm^2 system and compared them with the 1 cm^2 cell (Figure S24). The EIS results indicate that the observed EE loss arises from both increased ohmic resistance and the slowed kinetics and mass transport. The increase in ohmic resistance likely reflects longer in-plane current paths, higher contact resistance at the current collector/gas diffusion electrodes (GDE)/separator interfaces, and residual compression non-uniformity. Because ohmic losses scale with current (iR), these effects become more pronounced at the high total currents used here. On the anode, the Ti flow-plate oxidation under OER forms resistive surface films, while a non-optimized serpentine design promotes channeling and maldistribution, increasing concentration overpotentials and bubble-related transport losses. Further reductions in voltage are therefore expected from lowering contact/collector resistances (including Ti surface treatments or alternative materials), improving manifold and channel designs for uniform reactant transfer/product removal, tightening compression control, and refining the anode to mitigate transport and oxidation losses.

We also tested COR performance 800 cm^2 using a conventional AEM in an otherwise similar system. Across matched conditions, the separator-based cell consistently achieved higher C_2H_4 FE and lower full-cell voltage than the AEM setup (Figures 4F and 4G), aligning with performance trends observed at 1 cm^2. The separator-based cell reached EE values

Please cite this article in press as: Sun et al., Areal uniformity enables scaled separator-based CO electrolyzers, Joule (2026), https://doi.org/10.1016/j.joule.2026.102441

exceeding those of prior CO_2R/COR studies at the same scale (Figure S25), demonstrating the effectiveness of the rigid framing optimization over previous spacer-based approaches used to prevent membrane puncturing, as well as over CEM-based COR systems. Testing different anodes—NiFe-Ni foam versus commercial IrO_x—showed the NiFe-Ni foam markedly reduced cell voltage due to improved OER activity (Figure S26). Overall, the combined use of the hydrophilic separator, NiFe-Ni foam anode, and framing support lowered full-cell voltage, enabling performance at the 800 cm^2 scale.

We monitored electrolyte outlet temperature during operation and observed that cases with minimal current loss exhibited larger temperature rises as current increased, consistent with modest ohmic heating scaling with i^2R of the cell (Figure S27).[54]

To ensure thermal stability, we enhanced thermal management by implementing a larger radiator and increasing electrolyte volume, and evaluated system durability at 200 mA/cm^2 (160 A total) using the 800 cm^2 framing configuration (Figure S28). With these measures, the electrolyzer temperature remained below 25°C (Figure S5C), and both voltage and FE remained stable for more than 50 h (Figure S27).

Post-test analysis showed no mechanical degradation of the separator or GDE. Thickness measurements and structural characterization following stability tests—and across sealing ring, compressible gasket, and framing configurations—indicate that both components retained structural integrity, with no observable microstructural changes after operation (Figures S29–S31). No gas product crossover was detected during operation (Figures S10B and S32).

To assess possible contamination arising from anode dissolution followed by transport to the cathode and redeposition, we performed inductively coupled plasma optical emission spectroscopy (ICP-OES) analysis of the electrolyte, which detected minor Ni and Fe accumulation during operation (Figure S33C). We further analyzed the cathode GDE after 50 h using X-ray photoelectron spectroscopy (XPS). Samples taken from multiple locations showed only trace Ni and Fe on the cathode surface (Figures S33A and S33B). These minor deposits may have contributed to the slight decline in performance observed near the end of the 50-h operation.

Finally, we evaluated single-pass conversion efficiency (SPCE) (Figure 4H). Reducing the CO flow rate from 2 L/min to 0.71 L/min increased CO SPCE from 25% to 75%, with total FE remaining >90% and C_{2+} FE ~80%.

DISCUSSION

Scaling COR to large single-cell areas is essential for translating catalyst advances into plant-relevant throughputs and costs. In this work, we demonstrate COR at an 800 cm^2 scale by overcoming cell-area-dependent challenges of structure and sealing. Through a framing-based support design and separator architecture, we achieved uniform mechanical compression across an 800 cm^2 cell, restoring performance to near the lab-scale benchmark. We achieved 52% C_2H_4 FE, 125 A toward C_2H_4, and 192 A toward C_{2+} products.

More broadly, these results establish areal uniformity across the active area as a central engineering principle for scalable gas-fed electrolysis. In a large-area membrane-electrode-assembly, both under- and over-loading of local contact pressure degrade performance—under-loaded regions incur interfacial gaps and mass-transport/ohmic penalties, whereas over-loaded regions risk damage to thin components and efficiency loss. The framing/separator platform presented here offers a practical route to high-rate, energy-efficient COR at industrially relevant active areas, and provides a blueprint for extending these principles to other gas-to-molecule electrochemical technologies.

METHODS

Electrode preparation

Gas diffusion electrodes were fabricated by airbrushing a catalyst ink onto a commercial gas diffusion layer—carbon paper (Fuel Cell Store, Freudenberg H23C3). For the 800 cm^2 cell tests, the catalyst ink was prepared by mixing 2,000 mg of CuO nanoparticles (Sigma Aldrich, 544868) with 6 mL of Nafion dispersion (Fuel Cell Store, PFSA Dispersion D5, 5 wt%) and 36 mL of methanol. For 1 cm^2 (20 mg CuO + 60 μL Nafion + 3 mL methanol) and 50 cm^2 electrodes, the ink composition was scaled proportionally to maintain the same CuO-to-Nafion ratio. The resulting ink was sonicated in an ultrasonic bath for 2 h and then uniformly sprayed onto the gas diffusion layer using an airbrush to achieve a catalyst loading of ~1 mg/cm^2.

The NiFe-Ni foam anode was synthesized via heterogeneous nucleation following an established method.[25] Briefly, 285 g of nickel nitrate hexahydrate ($Ni(NO_3)_2{\cdot}6H_2O$) and 39 g of iron(II) sulfate heptahydrate ($FeSO_4{\cdot}7H_2O$) were separately dissolved in 4,800 mL of isopropanol (i-PrOH) and 1,600 mL of deionized water. The two solutions were then combined under vigorous stirring to form a homogeneous NiFe precursor solution. A precleaned nickel foam (20 cm × 40 cm) was fully immersed in this solution and maintained at 25°C for 24 h. After deposition, the foam was thoroughly rinsed with deionized water and dried in a vacuum oven at 25°C for 12 h to yield the NiFe-Ni foam anode (Figure S34).

System setup and sealing

COR electrochemical experiments were conducted in MEA cells with active areas of 1, 50, or 800 cm^2. Each cell featured a serpentine flow field on both the cathode and anode sides, fabricated from titanium (grade 2) for the cathode and anode. The MEA assembly included either a 35 μm-thick porous PTFE membrane (pore size 1 μm, porosity 83%, PTFE unlaminated membrane filters, hydrophilic, Sterlitech, H100A330R) used in separator configurations, a 50 μm-thick Sustainion 37–50 AEM in AEM-based configurations, or a Nafion 117 (Fuel Cell Store) for CEM. The membrane was positioned between a CuO-coated cathode and either a commercial Ir-mixed metal-oxide-coated titanium felt anode (Magneto Special Anodes) or a self-synthesized NiFe-Ni foam anode.

The 1 and 50 cm^2 cells were sealed with 254 μm silicone gaskets (High-Temperature silicone rubber sheet, 86435K121, McMaster-Carr) on both the cathode and anode sides. For the 800 cm^2 sealing ring-based configuration, the cell was sealed

using a 3/16″ Buna-N rubber sealing ring (Buna-N rubber, 9452K381, McMaster-Carr). For the 800 cm^2 gasket-based configuration, the cathode side was sealed using a 3/16″ Buna-N rubber sealing ring (Buna-N rubber, 9452K381, McMaster-Carr), while the anode side used a 1/32″ thick fluorosilicone rubber gasket (Chemical-Resistant fluorosilicone rubber sheet, 2183T22, McMaster-Carr). This sealing setup—comprising the sealing ring, gasket, and additional mechanical support—was designed to compensate for differences in electrode thickness and the depth of the flow field channels.

For anode gas analysis and OER testing, a gas-tight electrolyte reservoir was employed. This system utilized a PTFE tank sealed by compressing a flexible silicone cap (Figures S35–S38). To check the gas-tight integrity of the 800 cm^2 cell, all outlets were closed, and air was introduced at 10 psi; the system was considered gas-tight if pressure remained stable for 20 min.

In the framing-based setup, each structural layer was composed of rigid PTFE materials (Chemical-Resistant slippery PTFE sheet, 9266K21, McMaster-Carr) rather than compressible gaskets, as described in the main text. The thicknesses of the layers used in both the gasket and non-compressible framing setups are listed in Table S2.

To mitigate liquid product loss, a liquid trap was installed on the cathode side and a radiator on the anode side (Figures S8 and S9). The cathode-side liquid trap consisted of a sealed column containing 200 mL of deionized water and a single-pass valve to collect condensed liquid products. The anode-side cold trap comprised a stainless-steel radiator equipped with a fan, through which the electrolyte was circulated for condensation and recovery of volatile species.

The gap between the 800 cm^2 cell plates was measured using a vernier caliper. Ten positions across the cell were selected to evaluate uniformity (Figures 3B, 3D, and 4B). The change in the gap before and after cell assembly, denoted as Δt, was calculated as follows:

$$\Delta t = t_1 - t_1',$$

where t_1 is the gap between the 800 cm^2 cell plates before setup of cathode, anode, membrane, and anode support inside the cell; t_1' is the gap between the 800 cm^2 cell plates after the setup of all the components inside the cell.

Electrochemical measurements

The CO gas feed was supplied to the cell at flow rates of 20 sccm for the 1 cm^2 cell, 90 sccm for the 50 cm^2 cell, and 0.7–3 L/min for the 800 cm^2 cell using mass flow controllers (MFCs). For the 800 cm^2 system, MFC control was integrated via a data acquisition box that coupled the MFCs and the high-capacity power supply using a LabVIEW-based interface. The anolyte, consisting of 2 M NaOH, was delivered to the anode compartment at a flow rate of ~50 mL/min for 1 cm^2, ~200 mL/min for 50 cm^2, and ~5 L/min for 800 cm^2.

Electrochemical measurements were conducted in galvanostatic mode using either an electrochemical workstation (Autolab PGSTAT204) equipped with a 10 A booster or a programmable DC power supply (Magna-Power SL Series, 10 V, 250 A) for high-current operations.

The FE of the liquid and gas products was calculated as follows:

$$FE_{Liquids} = n_i \times \frac{z_i F}{Q} \times 100\%$$

$$FE_{Gas} = x_i \times v \times \frac{z_i F P_0}{RTI} \times 100\%,$$

where n_i is the number of moles of each liquid product, F is the Faraday Constant, z_i is the number of electrons transferred for each product, Q is the total charge passed during liquid product collection, x_i is the volume fraction of each gas product, v is the gas flow rate, P_0 is atmospheric pressure, R is the ideal gas constant, and T is the temperature.

The total partial current (TPC) to the target product is calculated by using the total current multiplied by the total FE toward the target product:

$$TPC_{Ethylene} = total\ current \times FE_{Ethylene} = Current\ Density \times total\ area \times FE_{Ethylene}.$$

The EE of the C_{2+} was calculated as follows:

$$EE_{C_{2+}} = \sum_i^n FE_i \times \frac{E_i^0}{E_{applied}}.$$

The SPCE was calculated as follows:

$$SPCE = \frac{CO\ consumption}{CO\ Input} \times 100\%.$$

Product analysis

The gas products generated from the COR reaction were analyzed using a gas chromatograph (PerkinElmer Clarus 590) equipped with a thermal conductivity detector and a flame ionization detector. The system employed a Molecular Sieve 5A capillary column and a packed Carboxen-1000 column, with argon used as carrier gas. Gas flow rates were quantified either using a bubble column, the water-displacement method, or a Coriolis mass flowmeter (Endress and Hauser).

Liquid products from the COR reaction were quantified via proton nuclear magnetic resonance spectroscopy (1H NMR). Liquid-phase products that crossed over to the anode side were sampled directly from the anolyte. Cathode-side liquid products were collected using a downstream liquid trap connected to the cathode gas outlet. This trap consisted of a column containing ~200 mL of deionized water at room temperature, into which the cathode gas stream was bubbled to dissolve and capture condensable species.

For NMR analysis, liquid samples were diluted with D_2O, and dimethyl sulfoxide was used as the internal standard. Spectra were acquired using an Agilent DD2 600 MHz NMR spectrometer operating in water-suppression mode.

RESOURCE AVAILABILITY

Lead contact

Requests for further information and resources should be directed to and will be fulfilled by the lead contact, David Sinton (dave.sinton@utoronto.ca).

Materials availability

All unique materials generated in this study are available from the lead contact upon reasonable request.

Data and code availability

All data supporting the findings of this study are available within this article and its supplemental information. Additional data is available from the authors on reasonable request. This study did not generate any code.

ACKNOWLEDGMENTS

This research was undertaken, in part, thanks to funding from the Canada Research Chairs Program (CRC-2021-00316) and the Natural Sciences and Engineering Research Council of Canada (NSERC) through the Alliance Program. The authors acknowledge the support of the Government of Canada's New Frontiers in Research Fund (NFRF), CANSTOREnergy project NFRFT-2022-00197. The authors also acknowledge support from TotalEnergies SE.

AUTHOR CONTRIBUTIONS

D.S., R.K.M., and E.H.S. supervised the project. P.S. and R.K.M. designed the experiments. P.S. carried out most of the system optimization and experiments with the help of R.K.M. P.S. and R.K.M. prepared the manuscript. C.P.O. assisted with the system setup and troubleshooting. H.S.M. assisted with catalyst preparation. T.D., R.A., and H.D. assisted with the mechanical components. Y.G. and P.P. assisted with the large cell experiments. J.L. assisted with the synthesis of the NiFe-Ni foam anode. P.V.S. and T.G. assisted with material preparation. J.Z. assisted with the NMR test for the liquid products. Y.C. assisted with the preparation of the electrode. All authors discussed the results and assisted during manuscript preparation.

DECLARATION OF INTERESTS

The authors declare no competing interests.

SUPPLEMENTAL INFORMATION

Supplemental information can be found online at https://doi.org/10.1016/j.joule.2026.102441.

Received: November 13, 2025
Revised: February 24, 2026
Accepted: March 31, 2026

REFERENCES

1. O'Brien, C.P., Miao, R.K., Shayesteh Zeraati, A., Lee, G., Sargent, E.H., and Sinton, D. (2024). CO(2) Electrolyzers. Chem. Rev. *124*, 3648–3693. https://doi.org/10.1021/acs.chemrev.3c00206.
2. da Cunha, S.C., and Resasco, J. (2024). Insights from Techno-Economic Analysis Can Guide the Design of Low-Temperature CO2 Electrolyzers toward Industrial Scaleup. ACS Energy Lett. *9*, 5550–5561. https://doi.org/10.1021/acsenergylett.4c02647.
3. Belsa, B., Xia, L., and García de Arquer, F.P. (2024). CO2 Electrolysis Technologies: Bridging the Gap toward Scale-up and Commercialization. ACS Energy Lett. *9*, 4293–4305. https://doi.org/10.1021/acsenergylett.4c00955.
4. Hirunsit, P., Senocrate, A., Gómez-Camacho, C.E., and Kiefer, F. (2024). From CO2 to Sustainable Aviation Fuel: Navigating the Technology Landscape. ACS Sustainable Chem. Eng. *12*, 12143–12160. https://doi.org/10.1021/acssuschemeng.4c03939.
5. Li, F., Thevenon, A., Rosas-Hernández, A., Wang, Z., Li, Y., Gabardo, C.M., Ozden, A., Dinh, C.T., Li, J., Wang, Y., et al. (2020). Molecular tuning of CO(2)-to-ethylene conversionMolecular tuning of CO2-to-ethylene conversion. Nature *577*, 509–513. https://doi.org/10.1038/s41586-019-1782-2.
6. Vass, Á., Endrődi, B., Samu, G.F., Balog, Á., Kormányos, A., Cherevko, S., and Janáky, C. (2021). Local Chemical Environment Governs Anode Processes in CO(2) Electrolyzers. ACS Energy Lett. *6*, 3801–3808. https://doi.org/10.1021/acsenergylett.1c01937.
7. Xie, K., Miao, R.K., Ozden, A., Liu, S., Chen, Z., Dinh, C.T., Huang, J.E., Xu, Q., Gabardo, C.M., Lee, G., et al. (2022). Bipolar membrane electrolyzers enable high single-pass CO(2) electroreduction to multicarbon products. Nat. Commun. *13*, 3609. https://doi.org/10.1038/s41467-022-31295-3.
8. Brückner, S., Feng, Q., Ju, W., Galliani, D., Testolin, A., Klingenhof, M., Ott, S., and Strasser, P. (2024). Design and diagnosis of high-performance CO_2-to-CO electrolyzer cells. Nat. Chem. Eng. *1*, 229–239. https://doi.org/10.1038/s44286-024-00035-3.
9. Jeanty, P., Scherer, C., Magori, E., Wiesner-Fleischer, K., Hinrichsen, O., and Fleischer, M. (2018). Upscaling and continuous operation of electrochemical CO2 to CO conversion in aqueous solutions on silver gas diffusion electrodes. J. CO2 Util. *24*, 454–462. https://doi.org/10.1016/j.jcou.2018.01.011.
10. Han, K., Rowley, B.C., Schellekens, M.P., Brugman, S., de Heer, M.P., Keyzer, L.P.S., and Corbett, P.J. (2024). Scaling the Electrochemical Conversion of CO2 to CO. ACS Energy Lett. *9*, 2800–2806. https://doi.org/10.1021/acsenergylett.4c00936.
11. Zhang, J., Jiang, M., Wang, C.S., Guo, K., Li, Q.X., Ma, C., Ni, S.F., Chen, G.Q., Zong, Y., Lu, H., et al. (2022). Transition-metal free C-N bond formation from alkyl iodides and diazonium salts via halogen-atom transfer. Nat. Commun. *13*, 7961. https://doi.org/10.1038/s41467-022-35613-7.
12. Ozden, A., Li, J., Kandambeth, S., Li, X.-Y., Liu, S., Shekhah, O., Ou, P., Zou Finfrock, Y., Wang, Y.-K., Alkayyali, T., et al. (2023). Energy- and carbon-efficient CO2/CO electrolysis to multicarbon products via asymmetric ion migration–adsorption. Nat. Energy *8*, 179–190. https://doi.org/10.1038/s41560-022-01188-2.
13. Wu, H., Huang, L., Timoshenko, J., Qi, K., Wang, W., Liu, J., Zhang, Y., Yang, S., Petit, E., Flaud, V., et al. (2024). Selective and energy-efficient electrosynthesis of ethylene from CO2 by tuning the valence of Cu catalysts through aryl diazonium functionalization. Nat. Energy *9*, 422–433. https://doi.org/10.1038/s41560-024-01461-6.
14. Goldman, M., Prajapati, A., Duoss, E., Baker, S., and Hahn, C. (2023). Bridging fundamental science and applied science to accelerate CO2 electrolyzer scale-up. Curr. Opin. Electrochem. *39*, 101248. https://doi.org/10.1016/j.coelec.2023.101248.
15. Ha, T.H., Kim, J., Choi, H., and Oh, J. (2024). Selective Zero-Gap CO2 Reduction in Acid. ACS Energy Lett. *9*, 4835–4842. https://doi.org/10.1021/acsenergylett.4c01410.
16. Burdyny, T., and Mulder, F.M. (2024). Scale-up of CO2 and CO electrolyzers. Joule *8*, 2449–2452. https://doi.org/10.1016/j.joule.2024.08.010.
17. Crandall, B.S., Ko, B.H., Overa, S., Cherniack, L., Lee, A., Minnie, I., and Jiao, F. (2024). Kilowatt-scale tandem CO2 electrolysis for enhanced acetate and ethylene production. Nat. Chem. Eng. *1*, 421–429. https://doi.org/10.1038/s44286-024-00076-8.
18. Ozden, A., Wang, Y., Li, F., Luo, M., Sisler, J., Thevenon, A., Rosas-Hernández, A., Burdyny, T., Lum, Y., Yadegari, H., et al. (2021). Cascade CO2 electroreduction enables efficient carbonate-free production of ethylene. Joule *5*, 706–719. https://doi.org/10.1016/j.joule.2021.01.007.
19. Kaczur, J.J., Yang, H., Liu, Z., Sajjad, S.D., and Masel, R.I. (2018). Carbon Dioxide and Water Electrolysis Using New Alkaline Stable Anion Membranes. Front. Chem. *6*, 263. https://doi.org/10.3389/fchem.2018.00263.
20. Wei, P., Gao, D., Liu, T., Li, H., Sang, J., Wang, C., Cai, R., Wang, G., and Bao, X. (2023). Coverage-driven selectivity switch from ethylene to acetate in high-rate CO(2)/CO electrolysis. Nat. Nanotechnol. *18*, 299–306. https://doi.org/10.1038/s41565-022-01286-y.
21. Endrődi, B., Kecsenovity, E., Samu, A., Darvas, F., Jones, R.V., Torok, V., Danyi, A., and Janáky, C. (2019). Multilayer Electrolyzer Stack Converts

Carbon Dioxide to Gas Products at High Pressure with High Efficiency. ACS Energy Lett. *4*, 1770–1777. https://doi.org/10.1021/acsenergylett.9b01142.

22. O'Brien, C.P., McLaughlin, D., Böhm, T., Xiao, Y.C., Edwards, J.P., Gabardo, C.M., Bierling, M., Wicks, J., Sedighian Rasouli, A., Abed, J., et al. (2024). Scalability and stability in CO2 reduction via tomography-guided system design. Joule *8*, 2903–2919. https://doi.org/10.1016/j.joule.2024.07.004.
23. Papangelakis, P., O'Brien, C.P., Shayesteh Zeraati, A., Liu, S., Paik, A., Nelson, V., Park, S., Xiao, Y.C., Dorakhan, R., Sun, P., et al. (2025). Scaled CO Electroreduction to Alcohols. Nat. Commun. *16*, 4969. https://doi.org/10.1038/s41467-025-59180-9.
24. Ayyub, M.M., Fődi, T., Endrődi, B., and Janáky, C. (2025). High performance CO reduction at electrolyzer stack level through system optimization. Carbon Energy *7*, e674. https://doi.org/10.1002/cey2.674.
25. Li, Z., Lin, G., Wang, L., Lee, H., Du, J., Tang, T., Ding, G., Ren, R., Li, W., Cao, X., et al. (2024). Seed-assisted formation of NiFe anode catalysts for anion exchange membrane water electrolysis at industrial-scale current density. Nat. Catal. *7*, 944–952. https://doi.org/10.1038/s41929-024-01209-1.
26. Subramanian, S., Kok, J., Gholkar, P., Sajeev Kumar, A., Iglesias van Montfort, H.-P., Kortlever, R., Urakawa, A., Dam, B., and Burdyny, T. (2024). CO residence time modulates multi-carbon formation rates in a zero-gap Cu based CO2 electrolyzer. Energy Environ. Sci. *17*, 6728–6738. https://doi.org/10.1039/d4ee02004a.
27. Endrődi, B., Samu, A., Kecsenovity, E., Halmagyi, T., Sebok, D., and Janaky, C. (2021). Operando cathode activation with alkali metal cations for high current density operation of water-fed zero-gap carbon dioxide electrolyzers. Nat. Energy *6*, 439–448. https://doi.org/10.1038/s41560-021-00813-w.
28. Smith, W.A., Burdyny, T., Vermaas, D.A., and Geerlings, H. (2019). Pathways to Industrial-Scale Fuel Out of Thin Air from CO2 Electrolysis. Joule *3*, 1822–1834. https://doi.org/10.1016/j.joule.2019.07.009.
29. Shih, A.J., Monteiro, M.C.O., Dattila, F., Pavesi, D., Philips, M., da Silva, A.H.M., Vos, R.E., Ojha, K., Park, S., van der Heijden, O., et al. (2022). Water electrolysis. Nat. Rev. Methods Primers *2*, 84. https://doi.org/10.1038/s43586-022-00164-0.
30. Terlouw, T., Bauer, C., McKenna, R., and Mazzotti, M. (2022). Large-scale hydrogen production via water electrolysis: a techno-economic and environmental assessment. Energy Environ. Sci. *15*, 3583–3602. https://doi.org/10.1039/d2ee01023b.
31. Creissen, C.E. (2025). Swapping membranes for separators. Nat. Energy *10*, 1183–1184. https://doi.org/10.1038/s41560-025-01833-6.
32. Deng, W., Xing, S., Maia, G.W.P., Wang, Z., Crandall, B.S., and Jiao, F. (2025). Diaphragm-based carbon monoxide electrolyzers for multicarbon production under alkaline conditions. Nat. Commun. *16*, 8444. https://doi.org/10.1038/s41467-025-63004-1.
33. Miao, R.K., Fan, M., Wang, N., Zhao, Y., Li, F., Liu, M., Arabyarmohammadi, F., Liang, Y., Ni, W., Xie, K., et al. (2025). CO electrolysers with 51% energy efficiency towards C2+ using porous separators. Nat. Energy *10*, 1197–1204. https://doi.org/10.1038/s41560-025-01846-1.
34. Lee, W.H., Kim, K., Lim, C., Ko, Y.-J., Hwang, Y.J., Min, B.K., Lee, U., and Oh, H.-S. (2021). New strategies for economically feasible CO2 electroreduction using a porous membrane in zero-gap configuration. J. Mater. Chem. A *9*, 16169–16177. https://doi.org/10.1039/d1ta03182a.
35. Wei, S., Hua, H., Zhao, Y., and Luo, J. (2025). Porous membranes enable selective and stable zero-gap acidic CO(2) electrolysers. Nat. Commun. *16*, 9299. https://doi.org/10.1038/s41467-025-64342-w.
36. Song, W., Xia, C., Zaman, S., Chen, S., and Xiao, C. (2024). Advances in Stability of NiFe-Based Anodes toward Oxygen Evolution Reaction for Alkaline Water Electrolysis. Small *20*, e2406075. https://doi.org/10.1002/smll.202406075.
37. Gong, L., Chen, J.J., and Mu, Y. (2017). Catalytic CO(2) reduction to valuable chemicals using NiFe-based nanoclusters: a first-principles theoretical evaluation. Phys. Chem. Chem. Phys. *19*, 28344–28353. https://doi.org/10.1039/c7cp06155b.
38. Wu, J., Ren, Z., Xu, X., Mok, D.H., Guo, W., Ye, K., Shen, P., Zhang, W., Ni, B., Wan, S., et al. (2024). Chemical Bath Deposition of NiFe Alloy Anode for Efficient Alkaline Water Electrolyzer Integration. Small *20*, e2407374. https://doi.org/10.1002/smll.202407374.
39. Sun, X., Shen, W., Liu, H., Xi, P., Jaroniec, M., Zheng, Y., and Qiao, S.Z. (2024). Corrosion-resistant NiFe anode towards kilowatt-scale alkaline seawater electrolysis. Nat. Commun. *15*, 10351. https://doi.org/10.1038/s41467-024-54754-5.
40. Jeon, S.S., Lim, J., Kang, P.W., Lee, J.W., Kang, G., and Lee, H. (2021). Design Principles of NiFe-Layered Double Hydroxide Anode Catalysts for Anion Exchange Membrane Water Electrolyzers. ACS Appl. Mater. Interfaces *13*, 37179–37186. https://doi.org/10.1021/acsami.1c09606.
41. Xu, Q., Garg, S., Moss, A.B., Mirolo, M., Chorkendorff, I., Drnec, J., and Seger, B. (2023). Identifying and alleviating the durability challenges in membrane-electrode-assembly devices for high-rate CO electrolysis. Nat. Catal. *6*, 1042–1051. https://doi.org/10.1038/s41929-023-01034-y.
42. Gu, Y., Park, D.-H., Kim, M.-H., Byeon, J.-H., Lim, D.-M., Park, S.-H., Kim, J.-H., Jang, J.-S., and Park, K.-W. (2024). NiFe layered double hydroxides synthesized based on solvent properties as anode catalysts for enhanced oxygen evolution reaction. Chem. Eng. J. *480*, 147789. https://doi.org/10.1016/j.cej.2023.147789.
43. Zhou, Y., Wang, Z., Cui, M., Wu, H., Liu, Y., Ou, Q., Tian, X., and Zhang, S. (2024). NiFe-Based Electrocatalysts for Alkaline Oxygen Evolution: Challenges, Strategies, and Advances Toward Industrial-Scale Deployment. Adv. Funct. Mater. *34*, 2410618. https://doi.org/10.1002/adfm.202410618.
44. Song, J.H., Ka, S., Lim, C., Han, M.H., Lee, D.K., Oh, H.-S., and Lee, W.H. (2023). Unveiling the anode reaction environment in a CO2 electrolyzer to provide a guideline for anode development. J. Mater. Chem. A *11*, 19312–19320. https://doi.org/10.1039/d3ta03774f.
45. Nelson, V.E., O'Brien, C.P., Edwards, J.P., Liu, S., Gabardo, C.M., Sargent, E.H., and Sinton, D. (2024). Scaling CO(2) Electrolyzer Cell Area from Bench to Pilot. ACS Appl. Mater. Interfaces *16*, 50818–50825. https://doi.org/10.1021/acsami.4c11103.
46. Edwards, J.P., Alerte, T., O'Brien, C.P., Gabardo, C.M., Liu, S., Wicks, J., Gaona, A., Abed, J., Xiao, Y.C., Young, D., et al. (2023). Pilot-Scale CO2 Electrolysis Enables a Semi-empirical Electrolyzer Model. ACS Energy Lett. *8*, 2576–2584. https://doi.org/10.1021/acsenergylett.3c00620.
47. Kibria, M.G., Edwards, J.P., Gabardo, C.M., Dinh, C.T., Seifitokaldani, A., Sinton, D., and Sargent, E.H. (2019). Electrochemical CO(2) Reduction into Chemical Feedstocks: From Mechanistic Electrocatalysis Models to System Design. Adv. Mater. *31*, e1807166. https://doi.org/10.1002/adma.201807166.
48. Gent, A.N. (1958). On the Relation between Indentation Hardness and Young's Modulus. Rubb. Chem. Technol. *31*, 896–906.
49. Baumgartner, L.M., Koopman, C.I., Forner-Cuenca, A., and Vermaas, D.A. (2022). Narrow Pressure Stability Window of Gas Diffusion Electrodes Limits the Scale-Up of CO(2) Electrolyzers. ACS Sustain. Chem. Eng. *10*, 4683–4693. https://doi.org/10.1021/acssuschemeng.2c00195.
50. Filippi, M., Möller, T., Pastusiak, R., Magori, E., Paul, B., and Strasser, P. (2024). Scale-Up of PTFE-Based Gas Diffusion Electrodes Using an Electrolyte-Integrated Polymer-Coated Current Collector Approach. ACS Energy Lett. *9*, 1361–1368. https://doi.org/10.1021/acsenergylett.4c00114.
51. Ha, M.G., Lim, C., Oh, C., Kim, H., Choi, J.-Y., Lee, W.H., and Oh, H.-S. (2024). Efficient and durable porous Membrane-Based CO2 electrolysis for commercial Zero-Gap electrolyzer stack systems. Chem. Eng. J. *496*, 154060. https://doi.org/10.1016/j.cej.2024.154060.

52. Rae, P.J., and Brown, E.N. (2005). The properties of poly(tetrafluoroethylene) (PTFE) in tension. Polymer *46*, 8128–8140. https://doi.org/10.1016/j.polymer.2005.06.120.

53. Mazur, K., Gądek-Moszczak, A., Liber-Kneć, A., and Kuciel, S. (2021). Mechanical Behavior and Morphological Study of Polytetrafluoroethylene (PTFE) Composites under Static and Cyclic Loading Condition. Materials (Basel) *14*, 1712. https://doi.org/10.3390/ma14071712.

54. Pelzer, H.M., Kolobov, N., Vermaas, D.A., and Burdyny, T. (2025). Scaling and heating will drive low-temperature CO2 electrolysers to operate at higher temperatures. Nat. Energy *10*, 549–556. https://doi.org/10.1038/s41560-025-01745-5.